Journal of Materials Research and Technology 33 (2024) 994–1003

Contents lists available at ScienceDirect

Journal of Materials Research and Technology

journal homepage: www.elsevier.com/locate/jmrt

Influence of phase transformation coefficient on thermomechanical modeling of laser powder bed fusion for maraging 300 steel

Bruno Caetano dos Santos Silva [a,b,*], Lucas de Figueiredo Soares [a,c], Rodrigo Santiago Coelho [a,c], Wojciech Sitek [d], Mariusz Król [d], Gilmar Ferreira Batalha [b]

[a] SENAI CIMATEC, Institute SENAI of Innovation for Forming and Joining of Materials, Av. Orlando Gomes, 1845, Piata, 41650-010, Salvador, BA, Brazil
[b] Department of Mechatronics and Mechanical Systems Engineering, Polytechnic School of Engineering, University of Sao Paulo, Av. Prof. Mello Moraes, 2231 Butanta, Sao Paulo, 05508-030, SP, Brazil
[c] University Center SENAI CIMATEC, Post-Graduation Program MPDS/GETEC/MCTI, Av. Orlando Gomes, 1845, Piata, 41650-010, Salvador, BA, Brazil
[d] Department of Engineering Materials and Biomaterials, Faculty of Mechanical Engineering, Silesian University of Technology, 18A Konarskiego St., 44-100, Gliwice, Poland

ARTICLE INFO

Handling Editor: L Murr

Keywords:
Laser powder bed fusion (LPBF)
Numerical simulation
Additive manufacturing (AM)
Maraging 300 steel (MS300)
Phase transformation

ABSTRACT

Manufacturing maraging steel components using laser-based powder bed fusion (LPBF) presents an attractive proposition for industries due to the material's combination of mechanical properties such as hardness, wear resistance, toughness and the capability to produce parts with complex geometries and high precision. Despite these advantages, the LPBF process induces defects such as distortion and residual stress associated with the complex thermal cycles, compromising final part quality. Numerical simulations have been developed to predict these defects. However, LPBF simulations remain challenging due to the complexity of the process and the substantial computational resources required. For maraging steel, for example, the occurrence of phase transformation promotes compressive stress that interferes in results and makes simulations inaccurate. This research aims to simulate a geometry with a circular inner channel and investigate distortion, volume fraction of martensite and equivalent stress results. Modeling was performed by varying phase transformation rate parameters to assess the impact of transformations on simulation outcomes. Results showed minimal impact of these parameters on distortions and equivalent stress. Equivalent stress results were compared with literature findings, while distortion results were validated against experimental data to validate the accuracy of the model.

1. Introduction

Maraging steel, characterized by its high nickel and low carbon contents, possesses a unique combination of properties crucial for various industrial applications. These properties include hardness, wear resistance, weldability, creep resistance and toughness [1–3]. The enhancement of maraging steel's properties is primarily attributed to the precipitation of intermetallic compounds [Ni_3Ti, Ni_3Mo, and $Ni_3(MoTi)$] within a martensitic microstructure. With a nickel content typically around 18%, maraging steel exhibits favorable machinability in its solution-annealed state and maintains dimensional stability during aging treatment [4,5]. The presence of dispersed retained austenite after quenching promotes the improvement of ductility and toughness [6,7]. All these characteristics combine with reduce thermal cracking due to the low carbon content, making maraging steel particularly well-suited for additive manufacturing (AM) processes [5,8].

The laser-based powder bed fusion (LPBF) technique has been employed in AM to produce parts made of maraging 300 steel (MS300) [9]. This technique consists in melting the powder feedstock of a desired region with a high-power and small spot-size laser, ensuring high resolution. The melting process occurs layer by layer until the final geometry is obtained [10]. LPBF provides various benefits to the industry, such as enabling the fabrication of intricate geometries and expediting rapid prototyping with high accuracy [11,12].

The intricate thermal dynamics inherent in LPBF processes, characterized by multiple rapid heating and cooling cycles reaching rates around 10^6 K/s, often lead to the formation of defects such as distortion and residual stress [13,14]. Various process parameters, including laser

* Corresponding author. SENAI CIMATEC, Institute SENAI of Innovation for Forming and Joining of Materials, Av. Orlando Gomes, 1845, Piata, 41650-010, Salvador, BA, Brazil.
E-mail address: bruno.silva@fieb.org.br (B.C.S. Silva).

https://doi.org/10.1016/j.jmrt.2024.09.034
Received 19 July 2024; Received in revised form 5 September 2024; Accepted 7 September 2024
Available online 10 September 2024

power, hatch spacing, layer thickness, and scan speed, play pivotal roles in defect formation [5]. To mitigate these challenges and minimize waste while expediting prototyping, numerical simulation solutions have been devised to predict these defects. However, simulating LPBF processes presents several challenges due to the complexity of thermal cycle models and the considerable computational resources required.

In response, ongoing research endeavors aim to address these challenges and advance the field of AM simulations. For instance, Baere et al. [15] delved into the distortions, residual stress, and phase transformation in MS300 cantilevers through numerical investigations. Their study involved a comparison of two effective laser power conditions and an analysis of their respective impacts on the outcomes. Similarly, Hanzl et al. [16] employed different software platforms to simulate intricate geometries using maraging steel and a nickel alloy, subsequently validating their results against experimental data. Papadakis et al. [17] undertook the manufacturing of MS300 molds for injection of thermoplastics using a holistic design approach. They conducted thermomechanical numerical simulations to predict distortion and compared their results with experimental 3D parts to validate the simulation outcomes. Additionally, studies focusing on 316 L stainless steel have contributed to a deeper understanding of simulation methodologies. Kaščák et al. [18] estimated the error of simulations through surface deviation methods using Simufact Additive commercial software. Similarly, Jin et al. [19] investigated simulations of annealing processing using 316 L stainless steel samples to predict the evolution of deformations and residual stress during this post treatment. Li et al. [20] developed a model to predict deformation and anticipate shape deviation. By producing a circular channel with various processing parameters, they identified the shape compensation that resulted in the most reduced dimensional deviation.

Despite the recent development on AM simulations, there are variations in the simulation process that should be better understood to obtain accurate results. Furthermore, as materials have different properties, they present different results, requiring specific studies. Simulations using MS300, for example, have some particularities such as phase transformation, which significantly influence the residual stress distribution within the geometry [15]. However, the literature lacks comprehensive studies elucidating the impact of phase transformation on simulations. In this scenery, this work aims to investigate the equivalent stress and distortion results in a geometry comprising circular channels simulated in MS300 through numerical modeling. The geometry was designed with focus on emerging applications of this material in the manufacturing of hot stamping tools with internal cooling channels. The model was implemented by Simufact Additive software varying a parameter that governs the phase transformation rate and validated through experimental data. This parameter serves as an estimate of the martensite and austenite transformation evolution [21]. In the simulation process, it is represented by a parameter referred to as the KM parameter.

2. Materials and methods

2.1. Numerical approach

The Inherent Strain Method (ISM) via finite element techniques in the commercial software Simufact Additive 2023 was employed to predict distortion, phase transformation and residual stress. This method is particularly advantageous for part-scale simulations, offering efficient prediction capabilities while significantly reducing computational time and costs. A thermomechanical analysis was carried out to assess both thermal history and mechanical aspects. This analysis is suggested for MS300 manufacturing, given the substantial impact of strain resulting from phase transformation, which is predominant in this material [6].

2.1.1. Governing equations

The thermomechanical approach involves conducting thermal analyses followed by mechanical analyses. Both analyses are independent and governed by different equations. In thermal calculations of ISM, thermal energy is applied to an entire layer, with heat conducted through adjacent layers using a simplified 3D heat transfer model based on the Fourier heat transfer equations and principles of energy conservation, as described in Equation (1) [15,22,23].

$$\rho C_p \frac{dT}{dt} = \frac{\partial}{\partial x}\left(k\frac{\partial T}{\partial x}\right) + \frac{\partial}{\partial y}\left(k\frac{\partial T}{\partial y}\right) + \frac{\partial}{\partial z}\left(k\frac{\partial T}{\partial z}\right) + Q \qquad \text{Equation 1}$$

Where: T represents temperature, t represents time, Q is the heat source and k stands for the thermal conductivity coefficient. Additionally, ρ and Cp represent density and specific heat capacity, respectively.

The outcome of the equation, determined by the specific geometry and boundary conditions, yields the temperature evolution of nodes and the thermal load applied to the structural analysis. As these loads induce stress, strains are determined through a mechanical analysis employing static equilibrium as dictated by Equation **(2)** and considering Hooke's law and classical J2 flow theory. Thermal strains, on the other hand, are derived using Equation **(3)** and then incorporated into the mechanical analyses [15,22–24].

$$\sum_i \frac{\partial \sigma_{ij}}{\partial x_i} = 0 \qquad \text{Equation 2}$$

$$\varepsilon_{th} = \alpha.\ \Delta T \qquad \text{Equation 3}$$

Where: σ_{ij} represents the stress acting in the x_i direction on a plane perpendicular to the x_j direction, ε_{th} is the thermal strain, α represents the temperature-dependent coefficient of thermal expansion, and ΔT denotes the temperature change during the process.

The result of mechanical analyses can be expressed by the summation of total strain evolution from different contributions, as shown in Equation (4) [25,26].

$$\varepsilon^{tot} = \varepsilon^{e} + \varepsilon^{p} + \varepsilon^{t} + \varepsilon^{phase} \qquad \text{Equation 4}$$

where ε^{tot} is the total strain, ε^{e} is the elastic strain, ε^{p} is the plastic strain, ε^{t} is the thermal strain and ε^{phase} is the transformational strain.

Since transformational strains are typically regarded as infinitesimal, their effects are often ignored by ISM. However, for MS300, such considerations cannot be neglected, and transformational strains must be accounted for and implemented accordingly [6]. These strains are derived from the evolution of temperature and are calculated based on the transformation of austenite in martensite, which promotes a volumetric expansion of 0.3% [15,27]. The prediction of transformational strain is based on the Koistinen-Marburger model (equation (5)), which requires information about the material such as martensite start temperature, as well as the KM parameter, representing the transformation rate [21,28,29].

$$f_{martensite} = f_{austenite}\ [1 - exp(\ -KM(M_s - T))] \qquad \text{Equation 5}$$

Where: $f_{martensite}$ and $f_{austenite}$ denote the volume fractions of martensite and austenite, respectively. M_s represents the martensite start temperature, and T is an arbitrary temperature.

2.1.2. Calibration steps

Thermomechanical analysis based on ISM requires a preliminary calibration step to ensure accurate results within a simplified approach. The calibration was conducted by measuring the experimental distortion after cutting the supports of a standard geometry, referred to as a cantilever, which is printed using the same process parameters as those used in the simulation. The distortion utilized in the calibration process involves the Z displacement that occurs after cutting the supports. Alzyod et al. [30] provide a detailed description of this calibration step.

For this work, an orthotropic setup was selected, as advised by the software developer. This approach distinguishes strains in the Y-

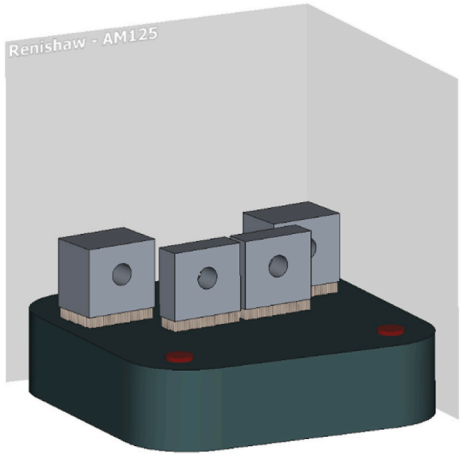

Fig. 1. Geometry designs used in the simulation.

Table 1
Overview of different simulated parameters.

Sample	Depth (mm)	KM Parameter
A10_0039	10	0.0039
A20_0039	20	0.0039
A10_0033	10	0.0033
A20_0033	20	0.0033
A10_0011	10	0.0011
A20_0011	20	0.0011

direction from those in the X-direction, requiring cantilevers to be printed in both directions. The outcome of the calibration step serves as input for simulating the specified geometry in the manufacturing phase, yielding distortion and residual stress results.

2.1.3. Geometry and mesh

The designed geometry for this study is depicted in Fig. 1. The modeling involved simulating four geometries, each with dimensions of 10 mm and 20 mm in depth. Each geometry features a circular straight channel with a nominal diameter of 8 mm, a height of 25 mm, and a width of 28 mm. The channels were designed without internal support.

An adaptive mesh was created as a strategy to reduce computational costs [31]. The geometry was divided into 29 element layers with a height of 1.0 mm. This configuration resulted in 69,624 voxels and 91, 669 nodes for the four geometries.

2.1.4. Simulation parameters

Since the simulation involving MS300 requires incorporation of phase transformation strain, three different KM parameters were utilized to evaluate their impact on the simulation results: 0.039, 0.033, and 0.011. This parameter governs the transformation rate of austenite to martensite. The first value was obtained by Equation (6), using martensite start and finish temperatures derived from experimental data [32,33]. Values of 0.033 and 0.011 parameters were recommended by the software database and drawn from previous works involving simulations of the same material in similar conditions [15], respectively. An overview of modeling parameters used in this study is provided in Table 1.

$$KM = -\ln(0,01) \,/\, (M_s - M_f) \qquad \text{Equation 6}$$

Where: Ms and Mf represent martensite start and finish temperatures, respectively.

To model the heat source, various parameters are required to calculate its magnitude, including scanning pattern, laser beam parameters, laser power, and absorption coefficient. These parameters are modeled through an effective laser power. For this simulation, an effective laser power value of 25% was used, based on results from previous literature that investigated the influence of this parameter [15].

Table 2
LPBF process parameters used for MS300.

Parameter	Value
Laser power (W)	200
Laser power scanning speed (mm/s)	350
Laser spot diameter (μm)	70
Hatch spacing (μm)	120
Layer thickness (μm)	30

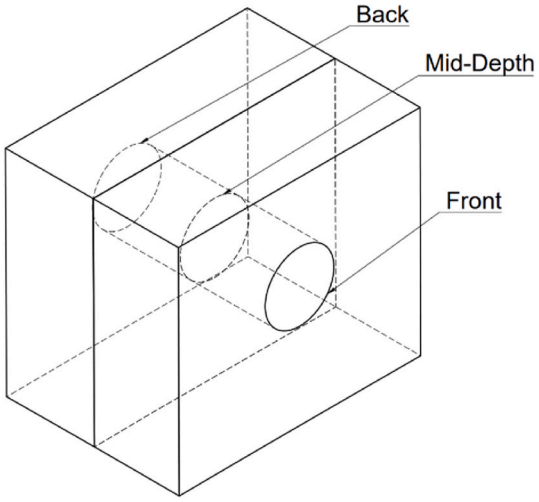

Fig. 2. Graphical representation of simulation validation measurements.

2.2. Experimental methods

The powder material utilized in this study was a gas-atomized 18Ni-300 maraging alloy (1.2709) provided by BÖHLER (Kapfenberg, Austria), with particle size ranging from 15 to 45 μm and spherical morphology. Further details regarding the material, including its chemical composition, are provided elsewhere [10].

The four geometries used in this study were fabricated using the AM125 system from RENISHAW (New Mills, UK), equipped with an Ytterbium (Yb) fiber laser with maximum laser power of 200 W, and wavelength of 1074 nm. Processing parameters used were those defined as optimal to maximize the density of MS300 parts processed by LPBF using the same feedstock in previous research [10]. These parameters are listed in Table 2.

2.3. Validation of simulation

Validation of the thermomechanical modeling was done by comparative analyses between simulated and experimental geometries. Given the critical importance of the channel within the part for the proposed application, its diameter was utilized as reference for validation. Printed parts were cut from the build plate and 3D-scanned with an ATOS Q system from Carl Zeiss GOM Metrology. The resulting diameter was calculated as an average of maximum circumscribed circles on front and back faces of the channel and at its mid-depth position as shown in Fig. 2, using the GOM Inspect Optical 3D software. The simulated dimension was obtained by plotting the maximum circumscribed diameter on the same positions of the channel using SolidWorks software.

An additional validation was conducted using a built-in geometry

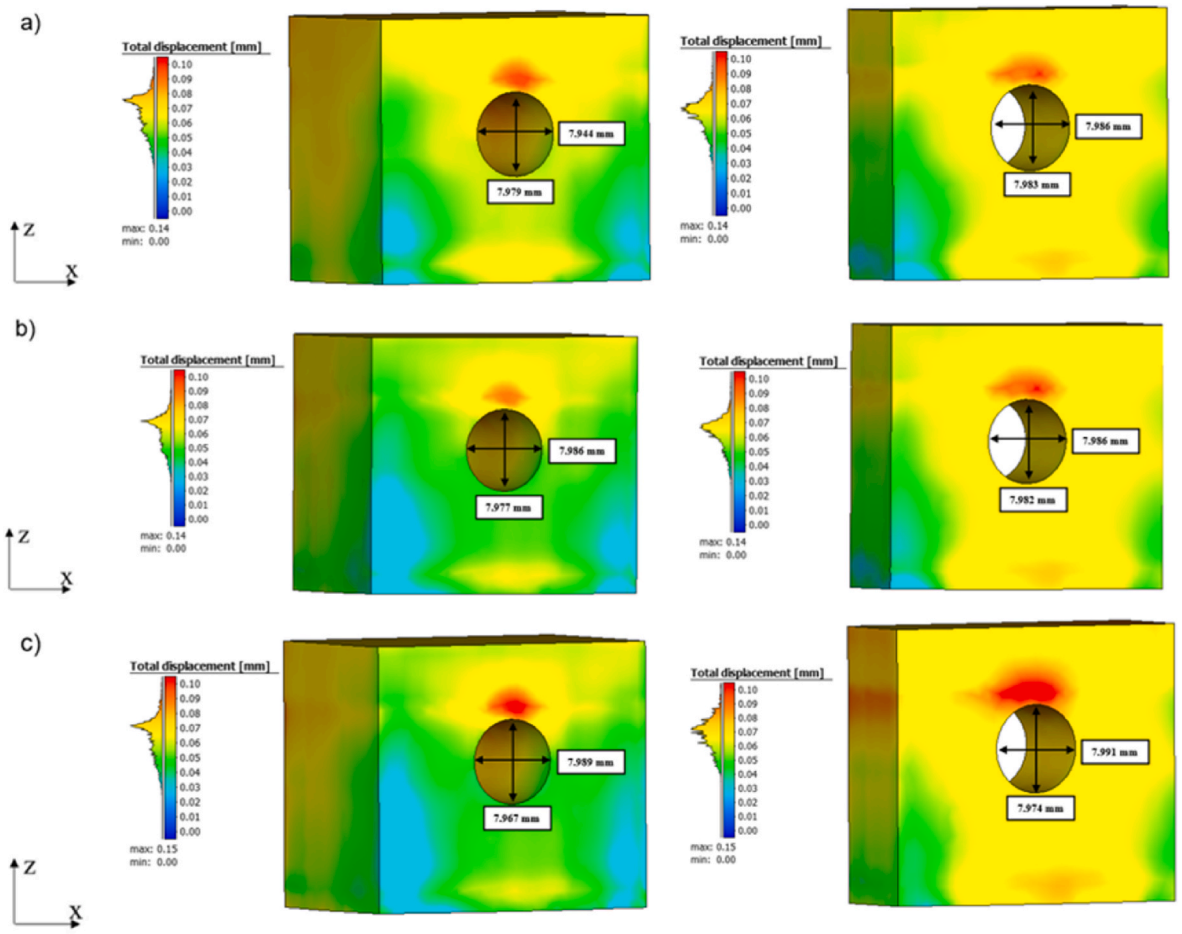

Fig. 3. Simulated displacement results using KM values of 0.039 (a), 0.033 (b), and 0.011 (c), with geometries of 20 mm and 10 mm depth on the left and right side, respectively.

inspection tool of Simufact Additive software. This tool functions by overlaying the scanned file with the simulated file, generating a surface deviation analysis to compare the similarity levels of both geometries.

3. Results and discussion

3.1. Numerical modeling

3.1.1. Distortion results

The distortion analysis of the channel's diameter was conducted and compared across different KM values, as illustrated in Fig. 3. The examination focused on the overall distortion behavior, illustrated by the color gradient, as well as the variation of the channel diameter in the X and Z directions.

Results revealed a consistent distortion pattern across the three models, characterized by higher levels of distortion at the top of the channel and a reduced horizontal diameter compared to the nominal measurement. The region corresponding to the X direction exhibited a consistent behavior with no significant gradient of distortion. However, despite its regular shape, the printed diameter in the horizontal direction was smaller than the designed form. This discrepancy is attributed to the accumulation of thermal stress on the channel surface, leading to distortion [34].

A red color gradient was observed at the top of the channel, indicating a higher level of distortion. This distortion can be attributed to the deflection mechanism, which promotes vertical diameter deformation (Z direction) [34]. During the layer deposition process, variations in heating and cooling rates lead to residual stress accumulation. These stresses cause the layers to warp upward, resulting in a deflection movement [35].

3.1.2. Phase distribution

Volumetric phase fraction results of the simulated geometries using different KM parameters are depicted in Fig. 4. Given that the KM parameter governs the phase transformation rate, a comparison was made between the volume fractions of martensite for each model. These findings are essential for MS300 due to its metastable microstructure, which induces phase transformation from martensite to austenite, with a consequent increment in strain and modification of the stress magnitude [28].

Phase transformation in MS300 is a complex process affected by various factors, including the heterogeneous concentration of elements like nickel, which promotes the austenite transformation, and temperature cycles resulting from manufacturing processes or heat treatment [28]. In this study, the modeling approach is solely dependent on temperature, with the formation of martensite purely based on cooling rates and martensitic start and finish temperatures. This approach could lead to overestimated results of volume fraction of martensite [15,36].

Volume fraction results in all cases show a predominantly martensitic microstructure with occasional regions containing austenite. These findings are consistent with previous investigations of phase transformations in MS300 manufactured by LPBF [37]. In their study, Conde et al. [37] reported an average austenite volume fraction of approximately 3% in as-built samples. Additionally, Kempen et al. [8] obtained a martensite fraction of 94.2% using a similar manufacturing process.

The comparative analysis of results for each model can contribute to

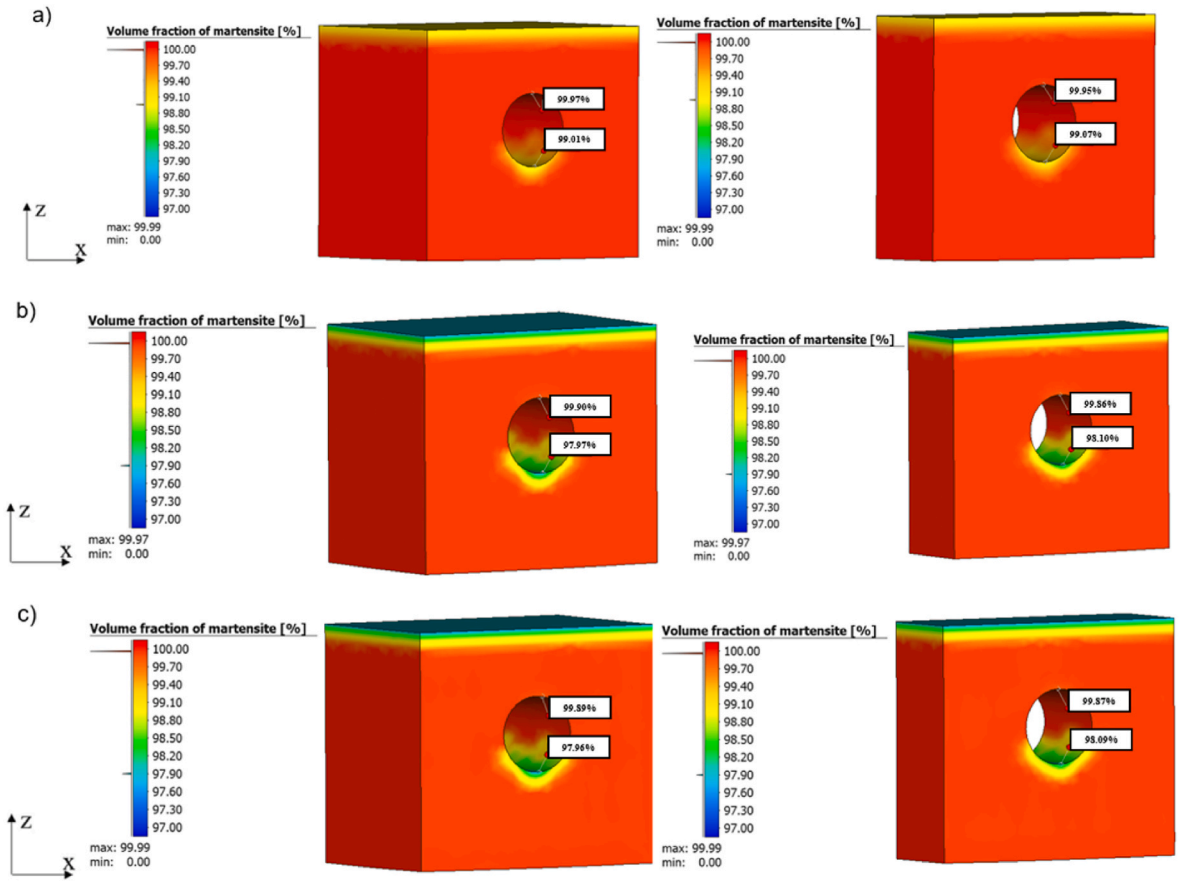

Fig. 4. Simulated martensite distributions using KM values of 0.039 (a), 0.033 (b), and 0.011(c), with geometries of 20 mm and 10 mm depth on the left and right side, respectively.

understanding the impact of this parameter on the precision of modeling. When comparing results using KM values of 0.039 and 0.033, a slight reduction in the martensite phase fraction was observed, from 99.01% to 97.97%, respectively, at the bottom of the channel. This variation implies that a smaller KM value results in greater difficulty in martensite formation. However, results obtained with a KM value of 0.011 did not show significant variation with respect to KM = 0.033, indicating the nonlinear influence of this parameter. It is important to note that these results may be overestimated because they are solely temperature-dependent, whereas in experimental processes, re-austenization depends on cooling rate and time [15].

Another significant aspect concerning the simulation outcomes of phase transformation pertains to the location of austenite formation. As previously noted, these calculations depend on simulated temperatures, with results derived from the temperature history generated during the thermal step. The occurrence of reverse austenite formation is typically associated with slower cooling rates, primarily occurring in reheated layers [15,37,38]. In LPBF process, the cooling rates of are too high and forms martensite even in the reheated layers. Chae et al. [39] identified the austenite formation in martensitic stainless steel just in the fourth heating cycle. However, in the edges of the geometry can cool down faster beyond the temperature range of the martensite transformation, forming austenite. In addition, the bottom of the channel and the top of the part were not submitted to a reheat process once there is no up layer, which could lead to austenite formation. This mechanism was also reported in previous literature [15].

3.1.3. Equivalent stress

The equivalent stress results using three different KM parameters are illustrated in Fig. 5.

The stress is essentially tensile along components. This stress behavior is formed due to the expansion of the melted layer that is restricted by the underlying solid substrate [40,41]. In particular, the inner surface of the channel shows significantly higher equivalent stress compared to adjacent areas. This increased stress is due to variations in heat dissipation mechanisms, which lead to differing cooling processes at the boundaries. In the boundary regions, thermal conduction is restricted to one side of the voxel, whereas in adjacent regions, conduction occurs from both sides. This difference results in distinct thermal cycles and stress distributions.

The equivalent stress on the inner surface of the channel was analyzed more carefully, as this region is critical to the study due to its heterogeneous behavior. Based on the simulation results, the equivalent stress at the bottom ranged between 160 and 205 MPa, while at the top of the channel, it was estimated to be about 470–620 MPa. The greater magnitude of stress at the top can be attributed to the restriction of distortion in this region. In a half channel, the distortion is expected to propagate upwards, but in the full channel this movement is restricted [34].

Experimental results of MS300 samples produced using LPBF have shown similar stress behavior. Mugwagwa et al. [42] reported tensile stresses ranging from 187 to 322 MPa, aligning with the peak observed in Fig. 5. Their study demonstrated that the magnitude of stress depends on the process parameters. Similarly, Santos et al. [43] found a tensile stress of 290 MPa on the surface of MS300 samples manufactured using comparable methods.

Variations in the KM parameter led to alterations in the equivalent stress behavior, especially when using KM = 0.011. In this case, the equivalent stress was notably higher. This result was expected, as the lower phase transformation parameter tends to promote the formation

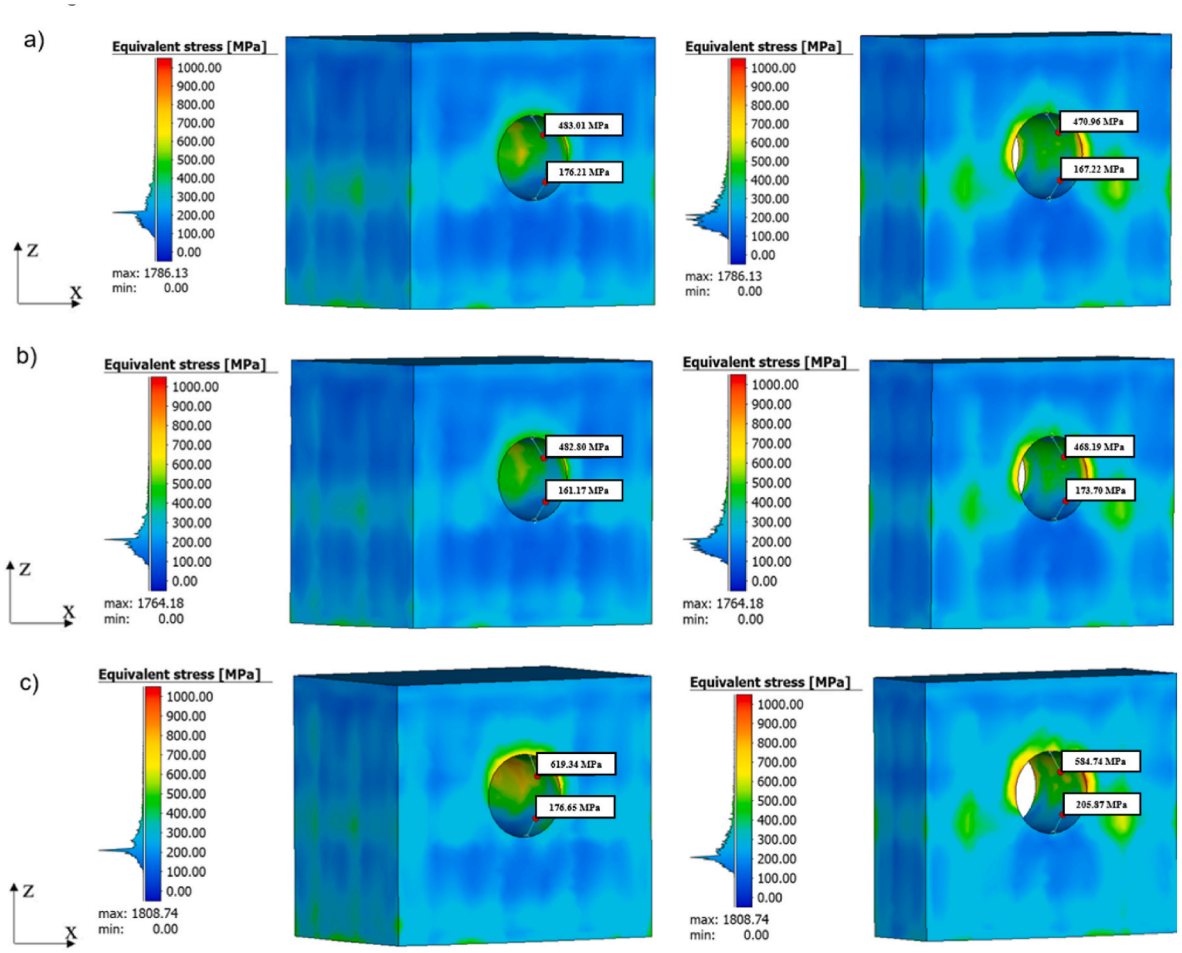

Fig. 5. Simulated equivalent stress results for KM values of 0.039 (a), 0.033 (b), and 0.011(c), with geometries of 20 mm and 10 mm depth on the left and right side, respectively.

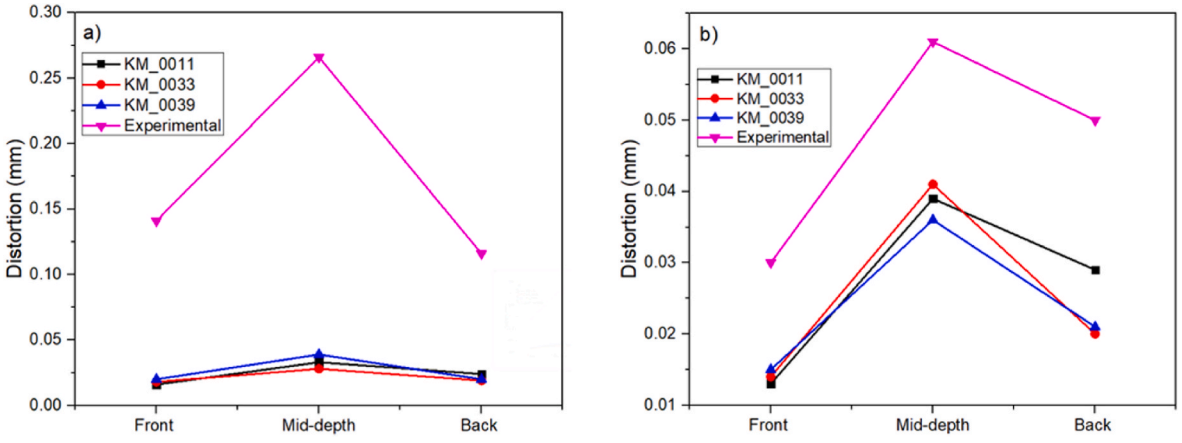

Fig. 6. Simulated and experimental distortions of the circumscribed circle on both faces and at the mid-depth position for depths of 10 mm (a) and 20 mm (b).

of more austenite, consequently inducing higher tensile stress. This finding contrasts the volume fraction results in section 3.1.2, which indicated similar volume fractions for models using KM = 0.011 and 0.033, leading to the expectation of similar equivalent stress in these two models. However, the volume fraction analysis was conducted at a single point, while equivalent stress can be influenced by the volume fraction across the adjacent regions. Mugwagwa et al. [42] and Baere et al. [15] reported these changes in the stresses of samples manufactured by LPBF influenced by the phase transformation.

Another observation from the equivalent stress analysis is the similarity in stress magnitude between the 10 mm and 20 mm geometries using the same KM parameter. Comparative analysis of localized equivalent stress in similar regions showed minimal variation, implying that the length of layers and the scale of the simulation have minimal impact on results. Therefore, multi-scale simulation could be a viable strategy for reducing computational costs to simulate larger geometries.

Table 3
Average of the three diameters of the channels.

Sample	Distortion Average
A10_0039	0,026 ± 0,011
A20_0039	0,024 ± 0,011
A10_0033	0,022 ± 0,006
A20_0033	0,025 ± 0,014
A10_0011	0,024 ± 0,009
A20_0011	0,027 ± 0,013

The efficacy of such a multi-scale strategy has been assessed in other studies [44,45]. Nonetheless, it is advisable to conduct further analysis using various scales to validate this approach.

3.2. Comparison between simulated and measured geometries and model validation

3.2.1. Influence of the KM parameter

Numerical simulation results varying the KM parameter were analyzed by comparing the distortion of the circumscribed circle at the three aforementioned positions, in parts with depths of 10 mm and 20 mm, as illustrated in Fig. 6(a) and (b), respectively. The distortion in the figure indicates the variation between the nominal and measured diameters. These values inferred a reduction of diameter in the simulated and printed geometry, once the dimensions were smaller than the nominal.

Simulated results indicate that the KM parameter exerts minimal influence on overall distortion. Distortions in each position presented similar values in both geometries for the three KM values evaluated. This observation can be ascribed to the limited impact of transformation strain on distortion, since the volume fraction of austenite phase is around 3%, and the volumetric transformation strain is limited to 0,003 [27,37]. Average distortions of the geometries are presented in Table 3. These results suggest a similar medium diameter for the three models, which indicates that the models exhibited similar distortion by standard deviation analysis. This result agrees with the previous analyses of the 3.1 section.

Similar distortion results were expected on front and back faces since they undergo similar thermal cycles, and the approach considers the deposition of an entire layer. However, variations in distortions were identified between these faces, which could be attributed to variations in the temperature gradient. This result is more noticeable in sample with depths of 20 mm. The mid-depth position displayed higher distortion when compared with the external faces, which can be attributed to differences in heating and cooling cycles in this region. The dissipation of heat is influenced by adjacent voxels, contributing to the observed variation. As the front and back faces are situated at the boundaries of the geometry, they present a distinct thermal conductivity mechanism influenced by the powder bed. This observation is corroborated by the experimental curve, which demonstrates a similar behavior.

Finally, simulated results lie closer to the experimental ones in the geometry with depth of 20 mm, while they deviate significantly from physical measurements for the 10 mm depth. Such difference should be the object of further investigation.

3.2.2. Surface deviation

The effect of the KM value on model accuracy was validated by comparing experimental and simulated geometries in terms of the circumscribed circle diameter of channels and surface deviation.

The comparison between printed and simulated circumscribed circle measurements is presented in Fig. 7. Deviations between simulated and printed diameters showed similar trends when comparing geometries with same dimensions. Notably, the 20 mm geometries exhibited lower deviations, suggesting that the models were more accurate for larger geometries. This result is clearly noted in the surface deviation scale, which is considerably lower in the 20 mm depth geometries.

The second step to validate the models was through surface deviation, as shown in Fig. 8. Qualitatively, results for models using different KM values look similar, based on color distribution. The color gradient of the 20 mm geometry presented a more regular behavior, presenting basically only one color and indicating the simulated models fit better to this geometry, corroborating previous results that reported more accurate results for the larger geometry.

Quantitatively, the surface deviation scale of the 20 mm geometry is more accurate, with an error predominately varying between −0.1 and 0.0 mm, while in the 10 mm geometry, the error varied between −0.1 and 0.1 mm in the surface and the channel of geometry. Despite this variation in both geometries, the deviation agrees with results presented in Table 3. The additional deviation indicated in the scale is attributed to dross formation at the top of the channel, which will be explained in the next paragraph, and the area where the geometry is cut from the base plate.

A deeper analysis of surface deviation at the top of the channel is presented in Fig. 9. This region is considered critical due to the presence of a surface irregularity known as dross formation observed in the printed specimens. The figure depicts the presence of this irregularity which reduces the vertical diameter. The color gradient is more pronounced, indicating that simulation did not predict this type of formation, regardless of the KM value used. Dahmen et al. manufactured similar geometries using LPBF in different positions and reported dross formation in this region. This formation, also known as an overhang structure in this type of geometry, was associated with the agglomeration of partially sintered or melted metal powder particles attached to channel walls [46,47].

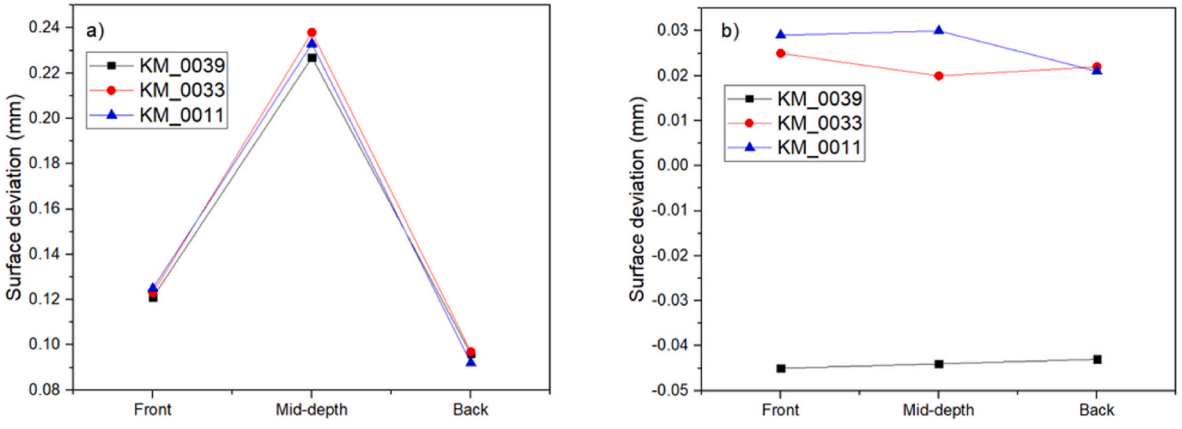

Fig. 7. Surface deviation of the circumscribed circle on both faces and at the mid-depth position for depths of 10 mm (a) and 20 mm (b).

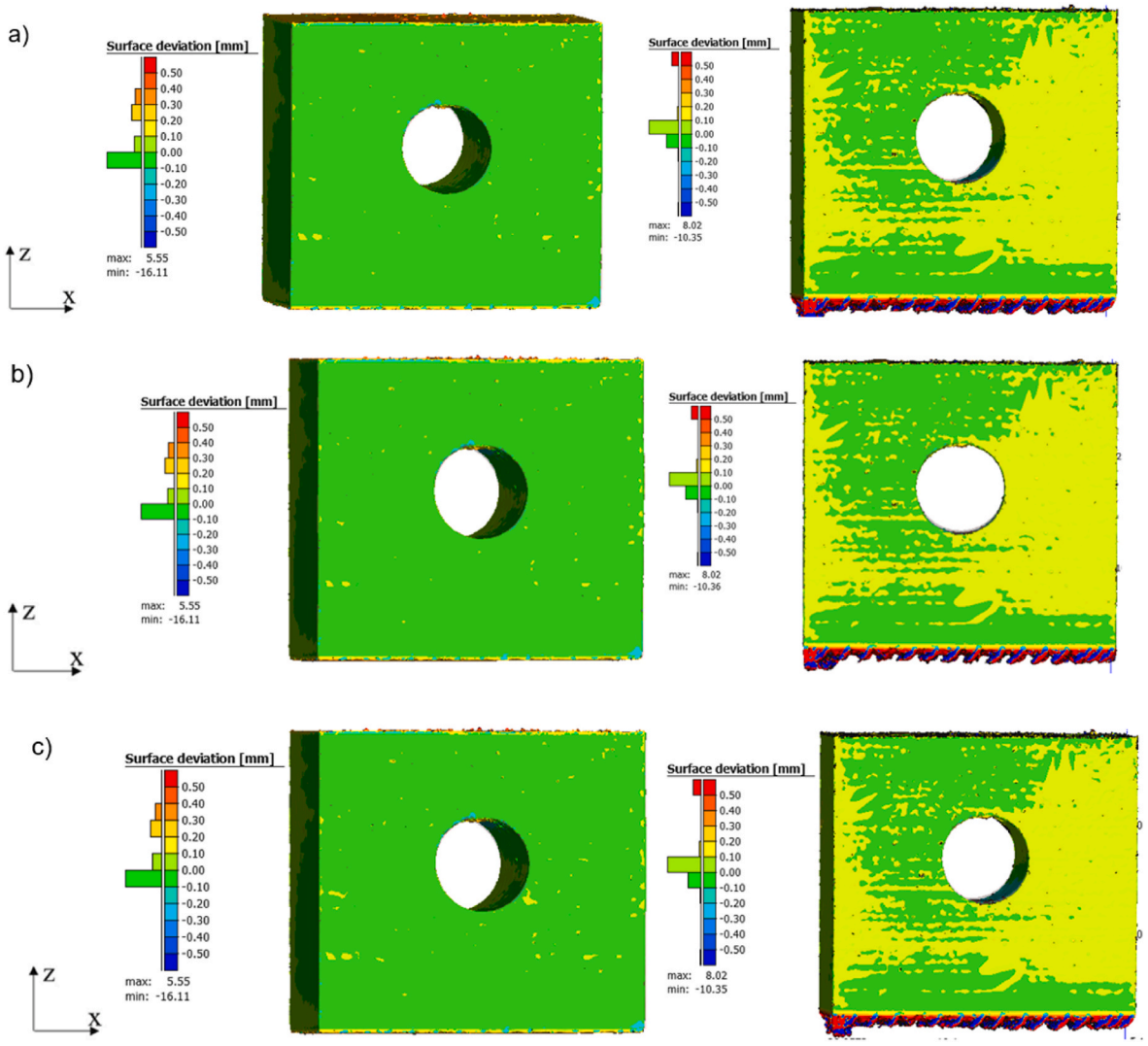

Fig. 8. Surface deviation results between simulated and printed geometries using KM values of 0.039 (a), 0.033 (b), and 0.011 (c) are shown, with geometries of 20 mm and 10 mm depth on the left and right side, respectively.

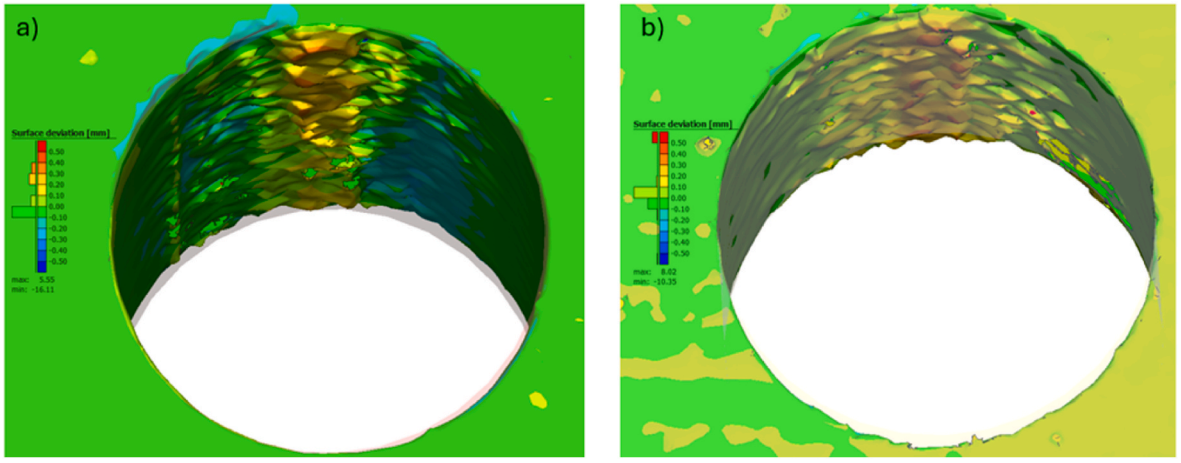

Fig. 9. Surface deviation analysis of the inner region of the channel using KM = 0.039 for the 20 mm (a) and 10 mm (b) geometries.

4. Conclusion

A finite element simulation was conducted to assess distortions, equivalent stress, and phase transformations in parts manufactured by LPBF, employing the inherent strain approach via a thermomechanical solution. The study focused on a geometry featuring an inner circular

channel made of MS300, a material undergoing extensive phase transformation during processing. Three models with varying phase transformation rate parameters (KM) were compared, alongside simulations of parts with different dimensions to evaluate model scalability.

The simulations revealed that the distorted geometries exhibited a reduced diameter compared to the nominal measurement, attributed to thermal stress-induced distortion primarily in the bordering regions during the LPBF process. The comparison of the three models with different KM parameters showed minimal variation, indicating that these parameters had no significant impact on overall deformation.

The prediction of martensite volume fraction indicated that lowers KM parameters resulted in a higher presence of austenite, due to the increased difficulty in martensite formation. This outcome exhibited a non-linear relationship, highlighting the complex interaction between KM parameters and phase formation. Equivalent stress analysis revealed a predominance of tensile stress within the geometry, with higher concentrations at the channel boundaries. Notably, the equivalent stress was greater at the top of the channel, likely due to restricted deformation in this region.

Model validation was performed by comparing simulated distortions with experimental data in two steps: first, by comparing specific measurements at three different points, and second, by assessing surface deviation between the simulated and experimental geometries. The models demonstrated high accuracy, with larger geometries yielding better results.

Declaration of generative AI and AI-assisted technologies in the writing process

During the preparation of this work the author(s) used ChatGPT in order to improve language and readability. After using this tool/service, the author(s) reviewed and edited the content as needed and take(s) full responsibility for the content of the publication.

Declaration of competing interest

The authors declare the following financial interests/personal relationships which may be considered as potential competing interests: Bruno Caetano dos Santos Silva reports equipment, drugs, or supplies was provided by Silesian University of Technology. If there are other authors, they declare that they have no known competing financial interests or personal relationships that could have appeared to influence the work reported in this paper.

References

[1] Moshka O, Pinkas M, Brosh E, Ezersky V, Meshi L. Addressing the issue of precipitates in maraging steels – unambiguous answer. Materials Science and Engineering: A. 2015;638:232–9. https://doi:10.1016/J.MSEA.2015.04.067.

[2] Dos Reis AG, Reis DAP, Abdalla AJ, Otubo J. High-temperature creep resistance and effects on the austenite reversion and precipitation of 18 Ni (300) maraging steel. Mater Char 2015;107:350–7. https://doi:10.1016/J.MATCHAR.2015.08.002.

[3] Casati R, Lemke J, Tuissi A, Vedani M. Aging behaviour and mechanical performance of 18-Ni 300 steel processed by selective laser melting. Metals 2016;6:218. https://doi:10.3390/met6090218.

[4] Tan C, Zhou K, Ma W, Zhang P, Liu M, Kuang T. Microstructural evolution, nanoprecipitation behavior and mechanical properties of selective laser melted high-performance grade 300 maraging steel. Mater Des 2017;134:23–34. https://doi:10.1016/J.MATDES.2017.08.026.

[5] Guo L, Zhang L, Andersson J, Ojo O. Additive manufacturing of 18% nickel maraging steels: defect, structure and mechanical properties: a review. J Mater Sci Technol 2022;120:227–52. https://doi:10.1016/j.jmst.2021.10.056.

[6] Wang MM, Tasan CC, Ponge D, Kostka A, Raabe D. Smaller is less stable: size effects on twinning vs. transformation of reverted austenite in TRIP-maraging steels. Acta Mater 2014;79:268–81. https://doi:10.1016/J.ACTAMAT.2014.07.020.

[7] Viswanathan UK, Dey GK, Asundi MK. Precipitation hardening in 350 Grade maraging steel. Metall Trans A 1993;24:2429–42. https://doi.org/10.1007/BF02646522.

[8] Kempen K, Yasa E, Thijs L, Kruth JP, Van Humbeeck J. Microstructure and mechanical properties of selective laser melted 18Ni-300 steel. Phys Procedia 2021;12:255–63. https://doi:10.1016/J.PHPRO.2011.03.033.

[9] Conde FF, Avila JA, Oliveira JP, Schell N, Oliveira MF, Escobar JD. Effect of the as-built microstructure on the martensite to austenite transformation in a 18Ni maraging steel after laser-based powder bed fusion. Addit Manuf 2021;46:102122. https://doi:10.1016/J.ADDMA.2021.102122.

[10] Król M, Snopiński P, Hajnyš J, Pagáč M, Łukowiec D. Selective laser melting of 18NI-300 maraging steel. Materials 2020;13:4268. https://doi:10.3390/ma13194268.

[11] Cooke S, Ahmadi K, Willerth S, Herring R. Metal additive manufacturing: technology, metallurgy and modelling. J Manuf Process 2020;57:978–1003. https://doi:10.1016/J.JMAPRO.2020.07.025.

[12] Blakey-Milner B, Gradl P, Snedden G, Brooks M, Pitot J, Lopez E, et al. Metal additive manufacturing in aerospace: a review. Mater Des 2021;209:110008. https://doi:10.1016/J.MATDES.2021.110008.

[13] Bai Y, Wang D, Yang Y, Wang H. Effect of heat treatment on the microstructure and mechanical properties of maraging steel by selective laser melting. Materials Science and Engineering: A. 2019;760:105–17. https://doi:10.1016/J.MSEA.2019.05.115.

[14] Liu S, Shin YC. Additive manufacturing of Ti6Al4V alloy: a review. Mater Des 2019;164:107552. https://doi:10.1016/J.MATDES.2018.107552.

[15] De Baere D, Moshiri M, Smolej L, Hattel JH. Numerical investigation into laser-based powder bed fusion of cantilevers produced in 300-grade maraging steel. Addit Manuf 2022;50. https://doi.org/10.1016/j.addma.2021.102560.

[16] Hanzl P, Zetková I, Daňa M, Nozar M. Advanced simulation of metal additive manufacturing using maraging steel and nickel alloy. Manufacturing Technology 2020;20:313–7. https://doi:10.21062/MFT.2020.045.

[17] Papadakis L, Avraam S, Photiou D, Masurtschak S, Pereira Falcón JC. Use of a holistic design and manufacturing approach to implement optimized additively manufactured mould inserts for the production of injection-moulded thermoplastics. Journal of Manufacturing and Materials Processing 2020;4:100. https://doi:10.3390/jmmp4040100.

[18] Kaščák Ľ, Varga J, Bidulská J, Bidulský R. Simulation of 316L stainless steel produced the laser powder bed fusion process. Materials 2023;16:7653. https://doi:10.3390/ma16247653.

[19] Jin QY, Kang D, Ha K, Yu JH, Lee W. Simulation of annealing process on AISI 316 L stainless steel fabricated via laser powder bed fusion using finite element method with creep. Addit Manuf 2022;60:103255. https://doi:10.1016/J.ADDMA.2022.103255.

[20] Li D, Liu X, Hou P, Liao H, Qi P, Nie R, et al. Deformation prediction and shape compensation model of circular channels using laser powder bed fusion. J Mater Res Technol 2023;27:3968–78. https://doi:10.1016/J.JMRT.2023.10.321.

[21] Erickson JS, Low JR. A general equation prescribing the austenite-martensite the extent of transformation iron-carbon in pure alloys and plain carbon steels. Acta Metall 1958;7:59–60. https://doi.org/10.1016/0001-6160(59)90170-1.

[22] Mohammadtaheri H, Sedaghati R, Molavi-Zarandi M. Inherent strain approach to estimate residual stress and deformation in the laser powder bed fusion process for metal additive manufacturing—a state-of-the-art review. Int J Adv Manuf Technol 2022;122:2187–202. https://doi:10.1007/s00170-022-10052-2.

[23] Hajializadeh F, Ince A. Short review on modeling approaches for metal additive manufacturing process. Material Design and Processing Communications 2020;2. https://doi:10.1002/mdp2.56.

[24] Dong W, Liang X, Chen Q, Hinnebusch S, Zhou Z, To AC. A new procedure for implementing the modified inherent strain method with improved accuracy in predicting both residual stress and deformation for laser powder bed fusion. Addit Manuf 2021;47:102345. https://doi:10.1016/J.ADDMA.2021.102345.

[25] Peter N, Pitts Z, Thompson S, Saharan A. Benchmarking build simulation software for laser powder bed fusion of metals. Addit Manuf 2020;36:101531. https://doi:10.1016/J.ADDMA.2020.101531.

[26] Wang Y, Li Q, Qian L, Yang Y. A modified inherent strain model with consideration of the variance of mechanical properties in metal additive manufacturing. J Manuf Process 2021;72:115–25. https://doi:10.1016/j.jmapro.2021.09.059.

[27] MSC. Volume A: theory and user information [Online]. Available: www.mscsoftware.com; 2008.

[28] Sjöström J, Durga A, Lindwall G. Linkage of macro- and microscale modeling tools for additive manufacturing of steels. Front Mater 2022;9. https://doi:10.3389/fmats.2022.797226.

[29] Kubiak M, Piekarsaka W, Domański T, Saternusa Z. Modelling of phase transformations in solid state and dilatometric curves using interpolation methods to determine CCT diagrams. Acta Phys Pol A 2022;142:184–7. https://doi:10.12693/APhysPolA.142.184.

[30] Alzyod H, Ficzere P. Using finite element analysis in the 3D printing of metals. Hungar J Ind Chem 2021;49:65–70. https://doi:10.33927/hjic-2021-24.

[31] Baiges J, Chiumenti M, Moreira CA, Cervera M, Codina R. An adaptive Finite Element strategy for the numerical simulation of additive manufacturing processes. Addit Manuf 2021;37:101650. https://doi:10.1016/J.ADDMA.2020.101650.

[32] Back JG. Modelling and characterisation of the martensite formation in low alloyed carbon steels. 2017.

[33] Król M, Snopiński P, Czech A. The phase transitions in selective laser-melted 18-NI (300-grade) maraging steel. J Therm Anal Calorim 2020;142:1011–8. https://doi:10.1007/s10973-020-09316-4.

[34] Feng S, Chen S, Kamat AM, Zhang R, Huang M, Hu L. Investigation on shape deviation of horizontal interior circular channels fabricated by laser powder bed fusion. Addit Manuf 2020;36:101585. https://doi:10.1016/J.ADDMA.2020.101585.

[35] Wang D, Mai S, Xiao D, Yang Y. Surface quality of the curved overhanging structure manufactured from 316-L stainless steel by SLM. Int J Adv Manuf Technol 2016;86:781–92. https://doi:10.1007/s00170-015-8216-6.

[36] Chadha K, Tian Y, Bocher P, Spray JG, Aranas C. Microstructure evolution, mechanical properties and deformation behavior of an additively manufactured maraging steel. Materials 2020;13:2380. https://doi:10.3390/ma13102380.
[37] Conde FF, Avila JA, Oliveira JP, Schell N, Oliveira MF, Escobar JD. Effect of the as-built microstructure on the martensite to austenite transformation in a 18Ni maraging steel after laser-based powder bed fusion. Addit Manuf 2021;46:102122. https://doi:10.1016/J.ADDMA.2021.102122.
[38] Belloli F, Demir AG, Previtali B. Understanding the deformation mechanisms of horizontal internal channels during the LPBF of 18Ni300 maraging steel. J Manuf Process 2021;71:237–48. https://doi:10.1016/J.JMAPRO.2021.07.063.
[39] Chae H, Huang E, Woo W, Kang S, Jain J, An K, et al. Unravelling thermal history during additive manufacturing of martensitic stainless steel. J Alloys Compd 2021; 857:157555. https://doi:10.1016/J.JALLCOM.2020.157555.
[40] Mercelis P, Kruth JP. Residual stresses in selective laser sintering and selective laser melting. Rapid Prototyp J 2006;12:254–65. https://doi:10.1108/13552540610707013.
[41] Liu Y, Yang Y, Wang D. A study on the residual stress during selective laser melting (SLM) of metallic powder. Int J Adv Des Manuf Technol 2016;87:647–56. https://doi:10.1007/s00170-016-8466-y.
[42] Mugwagwa L, Yadroitsev I, Matope S. Effect of process parameters on residual stresses, distortions, and porosity in selective laser melting of maraging steel 300. Metals 2019;9:16. https://doi.org/10.3390/met9101042.
[43] Santos LMS, Borrego LP, Ferreira JAM, de Jesus J, Costa JD, Capela C. Effect of heat treatment on the fatigue crack growth behaviour in additive manufactured AISI 18Ni300 steel. Theor Appl Fract Mech 2019;102:10–5. https://doi:10.1016/J.TAFMEC.2019.04.005.
[44] Gouge M, Denlinger E, Irwin J, Li C, Michaleris P. Experimental validation of thermo-mechanical part-scale modeling for laser powder bed fusion processes. Addit Manuf 2019;29:100771. https://doi:10.1016/j.addma.2019.06.022.
[45] Jimenez Abarca M, Darabi R, de Sa JC, Parente M, Reis A. Multi-scale modelling modeling for prediction of residual stress and distortion in Ti-6Al-4V Ti–6Al–4V semi-circular thin-walled parts additively manufactured by laser powder bed fusion (LPBF). Thin-Walled Struct 2023;182:110151. https://doi:10.1016/j.tws.2022.110151.
[46] Dahmen T, Klingaa CG, Baier-Stegmaier S, Lapina A, Pedersen DB, Hattel JH. Characterization of channels made by laser powder bed fusion and binder jetting using X-ray CT and image analysis. Addit Manuf 2020;36:101445. https://doi:10.1016/J.ADDMA.2020.101445.
[47] Pérez M, García-Collado A, Carou D, Medina-Sánchez G, Dorado-Vicente R. On surface quality of engineered parts manufactured by additive manufacturing and postfinishing by machining. Addit Manuf 2021:369–94. https://doi:10.1016/B978-0-12-818411-0.00015-X.